


Manipulation of Contact Angle Hysteresis at Electrified Ionic Liquid-Solid Interfaces

Pengcheng Nie^{1,2,*}, Xikai Jiang^{1,*}, Xu Zheng¹, and Dongshi Guan^{1,2,†}

¹*State Key Laboratory of Nonlinear Mechanics, Institute of Mechanics, Chinese Academy of Sciences, Beijing 100190, China*

²*School of Engineering Science, University of Chinese Academy of Sciences, Beijing 100049, China*

 (Received 1 August 2022; revised 27 March 2023; accepted 2 January 2024; published 25 January 2024)

Room-temperature ionic liquids (RTILs) are intriguing fluids that have drawn much attention in applications ranging from tribology and catalysis to energy storage. With strong electrostatic interaction between ions, their interfacial behaviors can be modulated by controlling energetics of the electrified interface. In this work, we report atomic-force-microscope measurements of contact angle hysteresis (CAH) of a circular contact line formed on a micron-sized fiber, which is coated with a thin layer of conductive film and intersects an RTIL-air interface. The measured CAH shows a distinct change by increasing the voltage U applied on the fiber surface. Molecular dynamics simulations were performed to illustrate variations of the solidlike layer in the RTIL adsorbed at the electrified interface. The integrated experiments and computations demonstrate a new mechanism to manipulate the CAH by rearrangement of interfacial layers of RTILs induced by the surface energetics.

DOI: [10.1103/PhysRevLett.132.044002](https://doi.org/10.1103/PhysRevLett.132.044002)

Room-temperature ionic liquids (RTILs) are unique electrolytes that consist purely of ions with large molecular size and strong ion-ion correlation. They have drawn much attention in a wide range of fields, from tribology and catalysis to energy storage, owing to their unique physical, chemical, and electrochemical properties [1–4]. They are also potentially a type of “active” liquids whose interfacial behaviors can be modulated by surface energetics and confinements [5–9]. Despite intensive research over recent decades, they have not reached their full potential in commercial batteries or supercapacitors, due to the lack of fundamental understanding of the molecular structure and fluid dynamics near electrified interfaces. Quantitative tools are needed to investigate their novel interfacial phenomena, which cannot be easily achieved with conventional liquids or dilute electrolytes, and gain new insights into their unique response to external mechanical and electrical cues.

One of the outstanding problems in interfacial dynamics is contact angle hysteresis (CAH) [10–14]. The pinning of three-phase contact line (CL) causes the contact angle θ between fluid interface and solid surface to depend on the direction of liquid motion, with advancing contact angle θ_a being larger than receding angle θ_r , resulting in a CAH,

$$F_h = \gamma(\cos \theta_a - \cos \theta_r), \quad (1)$$

where γ is the liquid-air interfacial tension. CAH is known to be very sensitive to surface defects resulting from physical roughness and/or chemical inhomogeneity. Recent studies demonstrate that CAH can be affected by modifications of the solid-liquid interface such as

reconstruction of polymer surfaces, adsorption and desorption of molecules, or formation of the electrical double layer [15–17]. Although considerable progress has been made recently in controlling the wettability of various solid surfaces [18,19], little is known on how to control the CAH of fluid interfaces moving on interested ambient solid surfaces [12,13], especially in the low velocity regime where the CAH is not attributed to inertial or viscous effects. Fully utilizing the molecular rearrangement of RTILs at electrified interfaces [20] would be a rational choice to this end.

In this Letter, we report a systematic study on the CAH of an RTIL over an electrified metallic surface. By tuning the voltage applied on the solid surface, it is found that CAH undergoes a change from almost zero to a large finite value, which is induced by variations of the solidlike layer (SLL) in the RTIL adsorbed at the electrified interface. In addition, our experiment demonstrates the capability of using CAH in capillary scale to detect molecular-scale adsorption and arrangement at electrified surfaces.

In the experiment, we use a recently developed “long-needle” atomic force microscope (AFM) [21–24] to directly measure the capillary force acting on a CL. As shown in Fig. 1, the long needle is made of a thin glass fiber coated by a layer of platinum (Pt) of thickness 20 nm [see Supplemental Material (SM) for more details [25]] and is immersed through a liquid-air interface, at which a circular CL is formed on the fiber surface. 1-ethyl-3-methylimidazolium acetate ([EMIM][OAc]) is used as the RTIL and held in a metal cell. The choice of [EMIM][OAc] is because it is one of the well-known RTILs [32] with a relatively large contact angle [33], and the large and asymmetric ions

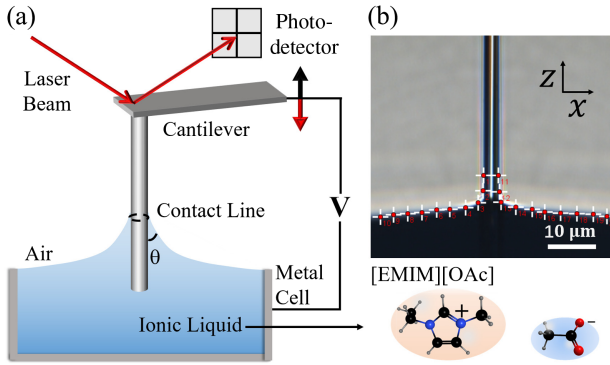


FIG. 1. (a) Sketch of the AFM-based capillary force apparatus at a liquid-air interface. The Pt-coated hanging fiber and the metal cell work as two electrodes and the RTIL is filled in between. (b) Optical image of the RTIL meniscus in the vicinity of a vertical fiber with a diameter $d = 3.5 \mu\text{m}$. Red dots indicate the meniscus profile. The coordinate system for image analysis and simulations is shown.

of imidazolium-based RTILs are essential for manipulating the CAH. The entire probe and cell are sealed by a closed fluid chamber to minimize evaporation and water adsorption. The fiber can move upward or downward through the liquid surface at a constant speed v and one can accurately measure the capillary force acting on the CL by AFM,

$$f_i = -\pi d \gamma \cos \theta_i, \quad (2)$$

in advancing (fiber moves downward, $i = a$) and receding (fiber moves upward, $i = r$) directions. Here, πd is the contact line length, $\gamma (\simeq 47 \text{ mN/m}$ for [EMIM][OAc] at 20°C) is the surface tension, and θ_i is the contact angle. The sign of f_i is defined as $f_i \leq 0$ for $\theta_i \leq 90^\circ$.

Figure 2 shows typical hysteresis loops of f_i and corresponding θ_i as a function of traveling distance s when the fiber is first pushed downward (advancing \rightarrow) and then is pulled upward (receding \leftarrow) through an RTIL-air interface. The initial loop measured during the first dipping event (black curve) is shown in Fig. 2(a). It consists of a sharp change of f on the left and right sides of the loop due to stretching of the liquid-air interface pinned on the fiber surface. When CL depins, it begins a stick-slip motion with the measured f fluctuating around a mean value f_i on the top and bottom of the loop. The large difference between the advancing capillary force f_a (top) and the receding one f_r (bottom) presents an obvious CAH, $F_h = (f_a - f_r)/\pi d$, for the RTIL on bare Pt surface. The following CAH loop measured with the same section of the fiber has a huge reduction ($s < s'$) during the second dipping (red curve). Until the fiber is pushed downward further ($s > s'$) where the RTIL-air interface meets the bare, never-wetted Pt surface, the measured f and θ increase with the travel distance s again. Figure 2(a) indicates that the RTIL is able to modify wetting properties and CAH of the bare

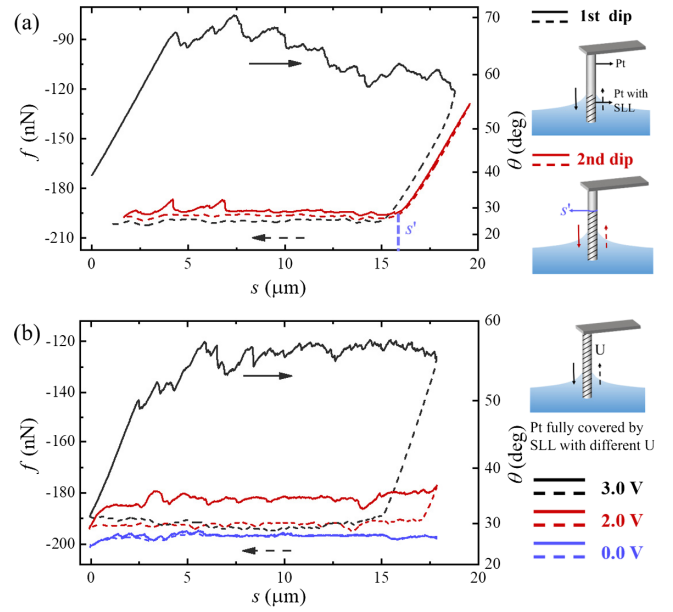


FIG. 2. (a) Variations of the measured capillary force f and corresponding θ as a function of traveling distance s during the first (black) and second (red) dips. Each hysteresis loop is measured when the fiber is first pushed downward (advancing \rightarrow , solid line) and then pulled upward (receding \leftarrow , dashed line) through an RTIL-air interface. Sketches on the right show experimental conditions. The shaded area on the fiber denotes prewetted surface with a SLL. s' denotes the position that divides bare Pt surface and SLL covered surface. (b) Measured hysteresis loops for different voltages $U = 0.0 \text{ V}$ (blue), 2.0 V (red), and 3.0 V (black) applied on the fiber surface. The measurements are made at a fixed fiber speed $v = 5 \mu\text{m/s}$ and with a fiber diameter $d = 1.5 \mu\text{m}$.

Pt surface. Successive CAH loops measured with the same section of the fiber are reproducible after the first dip, so our following measurements are made with a fiber fully prewetted by the RTIL.

Figure 2(b) shows a set of CAH loops measured at different voltages U applied on the fiber surface. It is seen that the advancing force (solid lines) increases with the applied voltage U , while the receding force (dashed lines) does not show a strong dependency on U . Therefore, the resulting CAH of this electrified interface depends on U . With a further increase in the voltage range applied on the probe, random large spikes appear in measured force loops when $U \geq 4 \text{ V}$ or $U \leq -1 \text{ V}$ (see Fig. S4 in SM [25]), indicating that electrochemical reaction occurs on the fiber surface. To avoid the electrochemical reaction, we conduct experiments within the measured stable electrochemical window ($\sim 4 \text{ V}$) in the current study.

Figure 3(a) shows the change of advancing and receding capillary force per unit length and contact angle as a function of voltage U with four different fiber diameters d . The four sets of data for d collapse onto common curves within experimental uncertainties and show a change of wetting behavior at $U \simeq 2.0 \text{ V}$. When the applied voltage

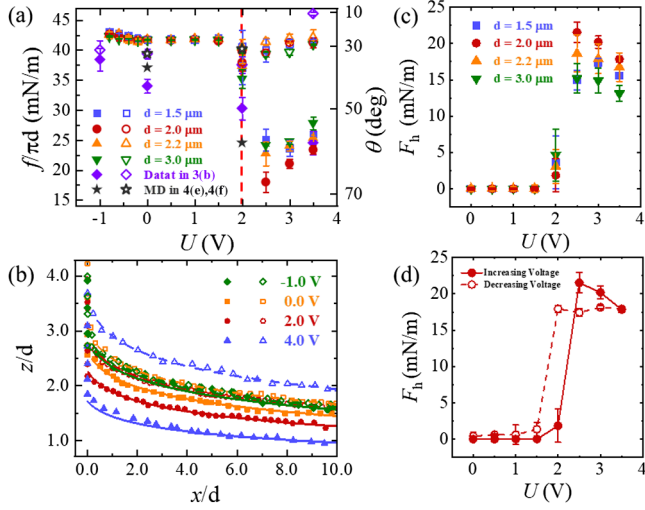


FIG. 3. (a) Measured capillary force per unit length $f/\pi d$ and the corresponding θ as a function of the applied voltage U during advancing (solid symbols) and receding (open symbols) processes. Four fibers with different diameters d are used in the experiment. Results from optical measurement [Fig. 3(b)] and MD simulations [Figs. 4(e) and 4(f)] are also shown. Error bars indicate standard deviations of the measurements at different positions on fiber. The dashed line indicates the threshold voltage. (b) Variations of the meniscus profile at different voltages U applied on the fiber in advancing (solid symbols) and receding (open symbols) directions measured by optical images [Fig. 1(b)]. The lines are fittings to Eq. (S1) in SM [25] with θ_i as the fitting parameter. (c) Measured CAH (F_h) as a function of U with different probes. (d) F_h measured with increasing or decreasing U .

$U < 2$ V, the advancing capillary force is almost equal to the receding one and thus there is little or negligible hysteresis (see Fig. S2 in SM [25]). For $U > 2.0$ V, the advancing capillary force deviates from the receding one with a change of contact angle of about 30° . Figures 3(c) and 3(d) further show the magnitude of CAH (F_h) as a function of U . It is seen that the change is sharp and the threshold voltage has a slight shift when F_h is measured with decreasing the applied voltage U . This threshold voltage shift is also observed when RTIL is taken as a liquid gate [7]. The CAH and threshold voltage do not depend on speeds v of the fiber investigated in the range of 0.5–100 $\mu\text{m/s}$.

To further verify variations of the measured f by AFM are due to changes of contact angle on the electrified fiber surface, we take optical microscope images of the RTIL meniscus in the vicinity of a vertical Pt-coated fiber, as shown in Fig. 1(b), in which red dots are used to mark the meniscus profile. Figure 3(b) shows normalized profiles of the RTIL meniscus near the fiber at different U in advancing and receding directions. Indeed, the profile, especially the height of the meniscus, changes with U . The corresponding contact angles θ_i are obtained by fitting the meniscus shape [25,34,35] and are shown in Fig. 3(a).

Despite limited spatial resolution along with relatively large experimental uncertainties in data extrapolation from optical images, the trend of θ_i as a function of U is consistent with that from AFM measurements. Compared with optical microscopy, the AFM-based capillary force apparatus directly measures interfacial forces modulated by U and captures dynamical hysteresis in the ultimate inner scale of a moving CL.

To understand the mechanism for manipulation of CAH at electrified RTIL-solid interface, molecular dynamics (MD) simulations are performed to investigate variations of molecular structures and interactions at the electrified interface between Pt and RTIL. More details about simulations are given in SM [25]. Figure 4(a) shows snapshots from MD simulations with ions in the two layers above Pt at $U = 0.0$ and 2.7 V, while Fig. 4(b) gives the

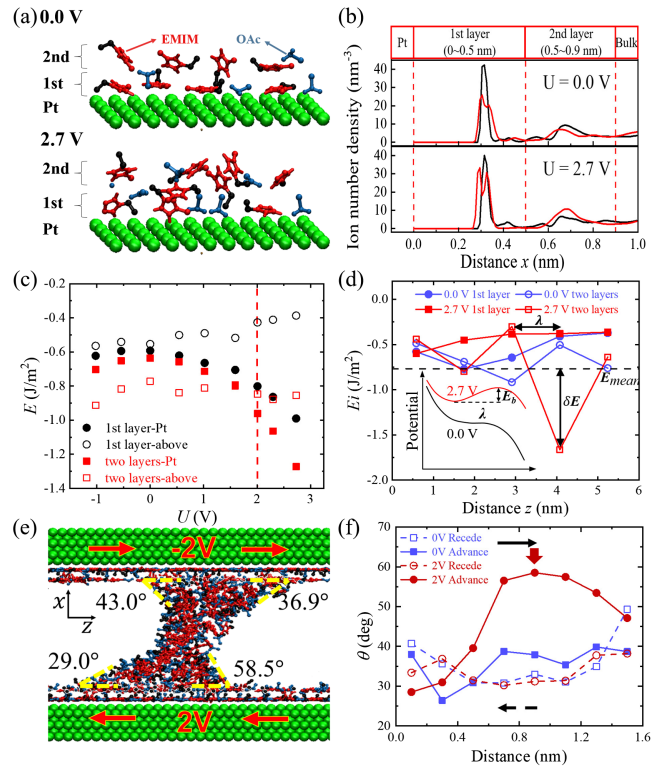


FIG. 4. (a) Snapshots from MD simulations showing ions in the two layers above Pt at $U = 0.0$ V (top) and 2.7 V (bottom). (b) Number density distribution of cation (black) and anion (red) as a function of distance x away from the Pt surface at $U = 0.0$ and 2.7 V. (c) Calculated interaction energy per unit area E between different regions as a function of U . The dashed line indicates the threshold voltage. (d) Energy in different subdomains shows enhanced fluctuations in the two layers at 2.7 V. The dashed line indicates the mean value E_{mean} of E_i in the two layers at 2.7 V. Inset shows the sketch of a pinning potential. (e) Snapshots from three-phase simulations showing θ_i and CAH at electrified surface $U = 2$ V (bottom). (f) Variations of θ in three-phase simulations show hysteresis loops for different U similarly to Fig. 2(b). The red arrow indicates the frame shown in (e), and the corresponding θ is plotted in Fig. 3(a).

corresponding distributions of cation and anion number densities. With an increase of U , rearrangement of ions takes place near the interface. For example, a double peak distribution of the anion number density appears in the first layer, as shown in Fig. 4(b), indicating that part of the anions prefer to bind with the highly charged Pt surface, while the others prefer to bind with cations. More anions migrate to the positive charged surface (Fig. S9 in SM [25]) and more cations are tilted [Fig. 4(a) herein and Fig. S8 in SM [25]]. Meanwhile, 2D pair correlation functions for ions in the first layer above Pt (Fig. S7 [25]) show this layer has solidlike behaviors, and ions in the layer have small diffusion coefficients ($D \simeq 0.018 \mu\text{m}^2/\text{s}$), which is about 15 times smaller than that in the bulk of the system. Experimental evidence based on AFM *in situ* imaging [5,36] and 3D mapping [37,38] techniques also demonstrates the U -dependent layered structures at RTIL-solid interfaces. Overall, the interfacial structures are rearranged and become more heterogeneous at $U = 2.7 \text{ V}$, which facilitates forming pinning sites to result in CAH.

The rearrangement of ions also causes variations of interaction energies. We calculate the interaction energies per unit area E by summing up pairwise Lennard-Jones and Coulombic potentials between ions in different regions, which are then divided by the cross-section (y - z plane) area of the simulation system, as shown in Fig. 4(c). It is found that the absolute value of E between Pt atoms and the first layer in the RTIL ($0 < x < 0.5 \text{ nm}$) is always larger than that between the first layer and ions above ($x > 0.5 \text{ nm}$) for different applied U considered in the experiment. Therefore, the RTIL is preferentially adsorbed on the Pt surface and forms a SLL once it touches Pt. This explains the reduction of CAH after the first dipping, as shown in Fig. 2(a), due to an adsorption of SLL on the Pt surface, and the RTIL-air interface tends to wet this SLL formed by itself. In contrast, E in the two layers above Pt shows a crossover at $U \simeq 2 \text{ V}$. The absolute value of E between the Pt atoms and the two layers ($0 < x < 0.9 \text{ nm}$) increases with U , while E between the two layers and the bulk liquid ($x > 0.9 \text{ nm}$) remains nearly constant (electrostatic interaction is screened by SLL), which leads to the crossover and indicates that the two layers tend to be adsorbed on the solid surface at $U \geq 2 \text{ V}$. Their energy difference ΔE at $U \simeq 2 \text{ V}$ is of the order of $\sim 0.10 \text{ J/m}^2$, which is about the same order as the adhesion energy $\gamma(1 + \cos \theta_0) \simeq 0.08 \text{ J/m}^2$ [13,39] measured from our AFM experiment, where the equilibrium contact angle θ_0 is taken $\theta_r \simeq 30^\circ$ as a reference state, since θ_r does not change much in different conditions. This threshold $U \simeq 2 \text{ V}$ also agrees with the voltage causing a change of CAH as shown in Fig. 3.

We have modeled CAH as an additional force required to overcome the energy barrier E_b between pinning and depinning states [22,23]. This barrier occurs due to the

variations in interfacial structures and energetics when U exceeds the threshold voltage. The value of $E_b \simeq f_c \lambda / 2b$, where f_c is the critical force acting on the pinning site to overcome the barrier, λ is a typical pinning size, and $b = 3/2$ for a generic linear-cubic potential [22,40]. To estimate E_b , the simulation system is equally divided along the z direction into multiple subdomains, with a width $\lambda = 1.16 \text{ nm}$ about twice the length of individual molecules [37]. Figure 4(d) shows typical energy E_i in different subdomains (i th). It is found that E_i varies significantly for ions in the two layers at 2.7 V , and the mean spatial fluctuation $\overline{\delta E} \simeq 0.19 \text{ J/m}^2$ is calculated by averaging $\delta E = E_i - E_{\text{mean}}$ over all subdomains and frames [25]. Then, we obtain $E_b \simeq 19.5 k_B T$, with $f_c \simeq \overline{\delta E} \lambda$. This E_b is very close to the capillary energy $E_c \simeq 18.7 k_B T$ estimated by a generic theory for CAH [10,16],

$$E_c = \gamma \lambda^2 [(\cos \theta_a - \cos \theta_0) / 2\theta_0]^2 \ln(\pi d / \lambda), \quad (3)$$

with all parameters directly from AFM experiments. Furthermore, for a given $E_c \simeq E_b$ induced by surface energetics, Eq. (3) predicts the hysteresis $F_h / \gamma = \cos \theta_a - \cos \theta_0$ decreases slightly as fiber diameter d increases, which is consistent with our experimental observation in Fig. 3(c). Therefore, we attribute the change of CAH to the variations in solid-liquid interfacial structures induced by the applied voltage, which gives rise to energy barriers that cost more dissipation when CL moves along the charged surface.

To further validate the integrated results from experiments and computations, we develop a three-phase simulation system for the RTIL meniscus between two parallel plates and measure CAH therein, as shown in Fig. 4(e). The plates move at a speed $u = 0.1 \text{ m/s}$ with a capillary number $\text{Ca} = u\eta/\gamma \approx 0.3$, which lies in the low-velocity regime and where surface tension still dominates as in our experiment. Figure 4(f) shows variations of θ at the advancing and receding CLs. We observe similar behavior in the hysteresis loops for different U , as compared to the experimental results [Fig. 2(b)]. Our MD simulations provide detailed information on surface energetics and enable one to have a quantitative understanding of the threshold voltage, adhesion energy, and energy barrier obtained from experimental data, based on the generic theory of wetting and CAH.

We expect the above features are also applicable to other imidazolium-based RTILs and charged surfaces. In the experiment, we also conducted measurements with other methylimidazolium-based RTILs on a Pt surface and [EMIM][OAc] on Au surface (see Fig. S5 in SM [25]). It is found that the U -dependent CAH emerges as expected while the threshold voltage and magnitude of the CAH are more sensitive to the RTIL type than metallic surface.

Finally, we discuss the fundamental differences between the conventional electrowetting of RTILs [41–43] and our study. First, electrowetting is the decrease in θ by applying a voltage drop between a droplet and a dielectric-covered electrode, whereas we find an increase in θ_a and CAH when the RTIL is directly placed on the electrode. Because the dielectric layer acts as a capacitor in the electrowetting system, solid-liquid interfacial energy is reduced and θ decreases as voltage increases. In contrast, Fig. 4(c) shows an increase of the interaction energy between the RTIL and the solid surface due to strong ion-ion correlation in the RTIL and electrostatic interaction between ions and the charged surface [44,45]. Second, a relatively large driving voltage (~ 50 – 200 V) is needed to achieve the electrowetting, except that an ultralow voltage electrowetting was reported for RTILs on an octadecyltrichlorosilane-coated silicon wafer [46]. In our study, a low voltage ($U \simeq 2$ V) is needed to modify interfacial structures, which is desirable for applications in microfluidics and nanotechnology. Third, electrowetting does not change the true contact angle but changes the curvature of the droplet and apparent θ , which are typically tens of microns to millimeters away from the contact region of three phases [47]. For our micron-sized needle AFM, it directly measures the capillary force acting on a CL; therefore, the variation of θ_i [Eq. (2)] is in the immediate vicinity of the contact line, where molecular interactions between the liquid and the solid are important.

This work was supported in part by NSFC under Grant No. 11972351 (D. G.), NSFC Basic Science Center Program for “Multiscale Problems in Nonlinear Mechanics” under Grant No. 11988102, and Chinese Academy of Sciences under Grant No. 025GJHZ2022023MI (X. J.).

*These authors contributed equally to this work.

[†]dsguan@imech.ac.cn

- [1] F. Zhou, Y. M. Liang, and W. M. Liu, *Chem. Soc. Rev.* **38**, 2590 (2009).
- [2] T. Welton, *Chem. Rev.* **99**, 2071 (1999).
- [3] M. C. Lin *et al.*, *Nature (London)* **520**, 325 (2015).
- [4] D. R. MacFarlane *et al.*, *Nat. Rev. Mater.* **1**, 15005 (2016).
- [5] R. Hayes, G. G. Warr, and R. Atkin, *Chem. Rev.* **115**, 6357 (2015).
- [6] A. Maali and B. Bhushan, *J. Phys. Condens. Matter* **20**, 315201 (2008).
- [7] J. T. Ye, Y. J. Zhang, R. Akashi, M. S. Bahramy, R. Arita, and Y. Iwasa, *Science* **338**, 1193 (2012).
- [8] J. Comtet, A. Niguès, V. Kaiser, B. Coasne, L. Bocquet, and A. Siria, *Nat. Mater.* **16**, 634 (2017).
- [9] A. Lainé, A. Niguès, L. Bocquet, and A. Siria, *Phys. Rev. X* **10**, 011068 (2020).
- [10] J. F. Joanny and P. G. de Gennes, *J. Chem. Phys.* **81**, 552 (1984).
- [11] L. Leger and J.-F. Joanny, *Rep. Prog. Phys.* **55**, 431 (1992).
- [12] E. L. Decker and S. Garoff, *J. Adhes.* **63**, 159 (1997).
- [13] D. Bonn, J. Eggers, J. Indekeu, J. Meunier, and E. Rolley, *Rev. Mod. Phys.* **81**, 739 (2009).
- [14] J. Snoeijer and B. Andreotti, *Annu. Rev. Fluid Mech.* **45**, 269 (2013).
- [15] H.-J. Butt, R. Berger, W. Steffen, D. Vollmer, and S. A. L. Weber, *Langmuir* **34**, 11292 (2018).
- [16] S. Franiatte, P. Tordjeman, and T. Ondarçuhu, *Phys. Rev. Lett.* **127**, 065501 (2021).
- [17] H.-J. Butt *et al.*, *Curr. Opin. Colloid Interface Sci.* **59**, 101574 (2022).
- [18] D. Quéré, *Annu. Rev. Mater. Res.* **38**, 71 (2008).
- [19] M. Ramiasa, J. Ralston, R. Fetzner, and R. Sedev, *Adv. Colloid Interface Sci.* **206**, 275 (2014).
- [20] S. N. Steinmann and Z. W. Seh, *Nat. Rev. Mater.* **6**, 289 (2021).
- [21] X.-M. Xiong, S. Guo, Z.-L. Xu, P. Sheng, and P. Tong, *Phys. Rev. E* **80**, 061604 (2009).
- [22] D. Guan, Y. J. Wang, E. Charlaix, and P. Tong, *Phys. Rev. Lett.* **116**, 066102 (2016).
- [23] D. Guan, Y. J. Wang, E. Charlaix, and P. Tong, *Phys. Rev. E* **94**, 042802 (2016).
- [24] D. Guan, E. Charlaix, and P. Tong, *Phys. Rev. Lett.* **124**, 188003 (2020).
- [25] See Supplemental Material at <http://link.aps.org/supplemental/10.1103/PhysRevLett.132.044002> for more details about experimental methods, simulation methods, and supplemental results, which includes Refs. [26–31].
- [26] H. Heinz, R. A. Vaia, B. L. Farmer, and R. R. Naik, *J. Phys. Chem. C* **112**, 17281 (2008).
- [27] M. Bahrami, M. H. Ghatee, and S. F. Ayatollahi, *J. Phys. Chem. B* **124**, 2835 (2020).
- [28] A. Arnold, O. Lenz, S. Kesselheim, R. Weeber, and C. Holm, *Meshfree Methods for Partial Differential Equations VI. Lecture Notes in Computational Science and Engineering* (Springer, Berlin, Heidelberg, 2013), 10.1007/978-3-642-32979-1_1.
- [29] A. Arnold, J. de Joannis, and C. Holm, *J. Chem. Phys.* **117**, 2496 (2002).
- [30] J. de Joannis, A. Arnold, and C. Holm, *J. Chem. Phys.* **117**, 2503 (2002).
- [31] L. Martinez, R. Andrade, E. G. Birgin, and J. M. Martinez, *J. Comput. Chem.* **30**, 2157 (2009).
- [32] X. J. Zhong, Z. P. Liu, and D. P. Cao, *J. Phys. Chem. B* **115**, 10027 (2011).
- [33] Z. Liu, T. Cui, G. Li, and F. Endres, *Langmuir* **33**, 9539 (2017).
- [34] Y. J. Wang, S. Guo, H.-Y. Chen, and P. Tong, *Phys. Rev. E* **93**, 052802 (2016).
- [35] S. Guo, X. Xu, T. Qian, Y. Di, M. Doi, and P. Tong, *J. Fluid Mech.* **865**, 650 (2019).
- [36] S. Liu, J. Peng, L. Chen, P. A. Sebastián, J. M. Feliu, J. Yan, and B. Mao, *Electrochim. Acta* **309**, 11 (2019).
- [37] S. Zhou, K. S. Panse, M. H. Motevaselian, N. R. Aluru, and Y. Zhang, *ACS Nano* **14**, 17515 (2020).
- [38] S. Benaglia, M. R. Uhlig, J. Hernández-Muñoz, E. Chacón, P. Tarazona, and R. Garcia, *Phys. Rev. Lett.* **127**, 196101 (2021).
- [39] E. Rolley and C. Guthmann, *Phys. Rev. Lett.* **98**, 166105 (2007).
- [40] A. Garg, *Phys. Rev. B* **51**, 15592 (1995).

- [41] S. Millefiorini, A. H. Tkaczyk, R. Sedev, J. Efthimiadis, and J. Ralston, *J. Am. Chem. Soc.* **128**, 3098 (2006).
- [42] M. Paneru, C. Priest, R. Sedev, and J. Ralston, *J. Am. Chem. Soc.* **132**, 8301 (2010).
- [43] L. Chen and E. Bonaccorso, *Adv. Colloid Interface Sci.* **210**, 2 (2014).
- [44] M. Z. Bazant, B. D. Storey, and A. A. Kornyshev, *Phys. Rev. Lett.* **106**, 046102 (2011).
- [45] G. Feng, J. Huang, B. G. Sumpter, V. Meunier, and R. Qiao, *Phys. Chem. Chem. Phys.* **13**, 14723 (2011).
- [46] X. N. Zhang and Y. G. Cai, *Angew. Chem. Int. Ed.* **52**, 2289 (2013).
- [47] Q. Ni and N. B. Crane, *Electrowetting Effect: Theory, Modeling, and Applications*. In *Wiley Encyclopedia of Electrical and Electronics Engineering*, edited by J. G. Webster (2015), [10.1002/047134608X.W8290](https://doi.org/10.1002/047134608X.W8290).